Engineering xxx (xxxx) xxx

Contents lists available at ScienceDirect

Engineering

journal homepage: www.elsevier.com/locate/eng

Research
Organoids and Organs-on-Chips—Article

Cerebral Organoid Modeling Reveals That Suppression of Aberrant mTOR Pathway Activation Alleviates Hyperbaric Oxygen-Induced Neurotoxicity

Xiaoying Ma [a,#], Ye Bai [b,#], Jiahui He [a,#], Yunxia Guo [a,c,#], Miao Meng [d], Sergey M. Novikov [e], Valentyn S. Volkov [e], Ilya Zavidovskiy [e], Dianhuai Meng [f], Yan Huang [a,*], Xiaochen Bao [b,*], Xiangwei Zhao [a,*]

[a] State Key Laboratory of Digital Medical Engineering, School of Biological Science and Medical Engineering, Southeast University, Nanjing 211189, China
[b] Department of Diving and Hyperbaric Medicine, Naval Medical Center, Shanghai 200433, China
[c] Department of Anesthesiology, The Affiliated Hospital of Yangzhou University, Yangzhou University, Yangzhou 225009, China
[d] Medical Operations Department Reception Office, Shanghai Sixth People's Hospital, Shanghai 200233, China
[e] Laboratory of Nanooptics and Plasmonics, Moscow Institute of Physics and Technology, Moscow 141701, Russia
[f] Rehabilitation Medical Center, The First Affiliated Hospital of Nanjing Medical University, Nanjing Medical University, Nanjing 210029 China

ARTICLE INFO

Article history:
Received 9 June 2025
Revised 26 August 2025
Accepted 22 October 2025
Available online xxxx

Keywords:
Cerebral organoid
Central nervous system oxygen toxicity
Hyperbaric oxygen therapy
Mammalian target of rapamycin pathway
Transcriptome sequencing

ABSTRACT

This study established human cerebral organoids as a promising platform for investigating central nervous system oxygen toxicity (CNS-OT). Through integrated transcriptomic, functional, and pharmacological analyses, we demonstrate that hyperbaric oxygen (HBO) exposure triggers pressure-dependent neurotoxicity mediated by the reactive oxygen species (ROS)–lysosome–mechanistic target of rapamycin (mTOR) axis. Key findings include the following: mechanistic hierarchy: Five atmospheres absolute (ATA) HBO induces metabolic dysregulation and cell cycle arrest, whereas six ATA exceeds compensatory thresholds, triggering overt apoptotic signatures; pathway crosstalk: Lysosomal permeabilization activates mTOR complex 1 (mTORC1) via cathepsin release, while mTORC1 hyperactivation suppresses transcription factor EB (TFEB)-mediated lysosomal regeneration, creating a self-amplifying loop; therapeutic potential: Mouse validation confirmed that mTOR inhibition (temsirolimus) attenuates neurotoxicity, with hippocampus-specific efficacy. The cerebral organoid model offers a human-relevant system to overcome species limitations in neurotoxicity research, facilitating mechanistic discovery and therapeutic target identification.

1. Introduction

Hyperbaric oxygen therapy (HBOT) involves breathing pure or highly concentrated oxygen under elevated pressure. Clinically, HBOT enhances oxygen diffusion into tissues, thereby mitigating hypoxia and aiding in wound repair [1,2]. However, experimental protocols and off-label applications—including military/industrial diving, cosmetic antiaging, and athletic recovery—carry heightened risks of oxygen toxicity [2].

Central nervous system oxygen toxicity (CNS-OT), characterized by convulsions, may occur when the inhaled oxygen partial pressure exceeds 200 kPa (~2 atmospheres absolute (ATA)) [3,4]. Risks escalate in diving medicine and decompression therapy, where exposures can reach 5–6 ATA (note: the pressure values of 5–6 ATA refer to oxygen partial pressure, not ambient air pressure). The mechanisms underlying CNS-OT remain elusive, although proposed hypotheses involve neurotransmitter dysregulation [5], oxidative stress [6,7], and aberrant adenosine metabolism [8]. A lack of systematic molecular investigations has hindered the development of targeted clinical interventions, severely limiting the utility of HBOT in critical care and extreme-environment medicine [9].

HBOT has similar clinical indications in both pediatric and adult populations, with children often exhibiting faster and more pronounced therapeutic responses. However, the unique developmental processes in children render HBOT research particularly distinctive in this population [10]. Progress in this field has been

* Corresponding authors.
E-mail addresses: hylucky@seu.edu.cn (Y. Huang), zhouqybb@163.com (X. Bao), xwzhao@seu.edu.cn (X. Zhao)..
# These authors contributed equally to this work.

https://doi.org/10.1016/j.eng.2025.10.020

Please cite this article as: X. Ma, Y. Bai, J. He et al., Cerebral Organoid Modeling Reveals That Suppression of Aberrant mTOR Pathway Activation Alleviates Hyperbaric Oxygen-Induced Neurotoxicity, Engineering, https://doi.org/10.1016/j.eng.2025.10.020

constrained by model limitations [11]. Ethical considerations and safety protections preclude direct toxicological studies on developing human brains. While numerous animal models have been employed in research, the existing evidence remains insufficient to establish their physiological relevance to humans [12]. Marked interspecies differences result in divergent differentiation trajectories and mechanisms compared with those in humans. On the other hand, while animal models enable the evaluation of overall survival rates post-HBO exposure, quantitative analysis of seizure activity, and observation of neuropathological alterations via histological sections alongside cerebral hemodynamic measurements, precise attribution of these responses to specific cell types—such as neurons, astrocytes, or vascular cells—requires targeted cellular labeling and often necessitates supplementary validation through *in vitro* culture systems [13,14]. Conventional two-dimensional cell cultures also fail to accurately predict *in vivo* responses because of their lack of physiological microenvironments and complex cell cell interactions [15,16].

Cerebral organoids have emerged as powerful models that faithfully recapitulate fetal brain development in terms of morphogenesis, genetic signatures, and gene expression profiles [17]. These three-dimensional constructs have been successfully implemented in mechanistic investigations of neurodevelopmental disorders (e.g., microcephaly [18]), neurodegenerative diseases [19,20], and heavy metal neurotoxicity [21]. However, their application in HBO-induced CNS-OT research has not yet been systematically explored.

Hence, in this study, human embryonic stem cell-derived cerebral organoids were used to establish an *in vitro* model of HBO-induced CNS-OT. Through transcriptome sequencing analysis, we systematically characterized oxygen toxicity-associated gene expression changes and identified potential key regulatory pathways using bioinformatics approaches (Fig. 1). Furthermore, we validated the molecular mechanisms in murine *in vivo* models and evaluated the neuroprotective efficacy of targeted pharmacological interventions. This cerebral organoid-based methodology provides unprecedented opportunities for investigating human-specific neurotoxic responses while overcoming the limitations of conventional model systems. Our findings advance the mechanistic understanding of CNS-OT pathogenesis and facilitate the development of targeted neuroprotective strategies.

2. Materials and methods

2.1. Human embryonic stem cells (hESCs) culture

ESCs (H9, provided by Stem Cell Bank, Chinese Academy of Sciences, China) were cultured in mTeSR™Plus (Stemcell Technologies, Canada) on Matrigel-coated six-well plates and passaged every 5–6 d.

2.2. Cerebral organoid culture

2.2.1. Embryoid body (EB) formation

When cell confluence reached 80%, 1 mL of gentle cell dissociation reagent (1000485; Stemcell Technologies) was added and incubated at 37 °C for 8 10 min. The reaction was then terminated by adding 1 mL of mTeSR™Plus medium (1000274; Stemcell Technologies), and the cells were collected. After centrifugation at 300*g* for 5 min, the supernatant was discarded, and the cell pellet was resuspended in 1 mL of EB formation medium supplemented with 10 μmol·L^{-1} Y-27632 (72304; Stemcell Technologies). The cells were gently pipetted to generate a single-cell suspension. A volume of 100 μL of cell suspension (9000 cells per well) was seeded into each well of a 96-well round-bottom ultra-low attachment plate (7007; Corning, USA). The plate was kept undisturbed for 24 h to allow EB formation. On days 2 and 4, 100 μL of EB formation medium was added to each well.

2.2.2. Induction of differentiation

On day 5, EBs with smooth and intact edges were carefully transferred using a wide-bore 200 μL pipette tip into induction medium (08570; Stemcell Technologies). Prior to the procedure, 9–12 embedding surfaces were prepared using parafilm and tip-rack holes, sterilized with ethanol, and exposed to ultraviolet (UV) light for aseptic processing. After 48 h, when the structures exhibited a radial translucent morphology, they were transferred onto the pre-formed embedding surfaces. Then, 15 μL of Matrigel solution was added dropwise to each structure and incubated at 37 °C for 30 min to allow solidification. Finally, the embedded structures were transferred into expansion medium (08570; Stemcell Technologies) for further culture. On day 10, the medium was replaced with mature medium (08571; Stemcell Technologies) and transferred to a shaker for incubation. The medium was replaced with fresh medium every three days.

2.3. Reverse transcription quantitative real-time polymerase chain reaction (RT-qPCR)

Total messenger RNA (mRNA) was extracted from organoids or ESC using Trizol reagent (Sango Biotech, China). Complementary DNA (cDNA) was synthesized from 500 ng of RNA using PrimeScript™ RT master mix (TAKARA, Japan). PCR amplification was performed with PrimeSTAR max premix (2×) (TAKARA). PCR condition: 2 min at 98 °C, then 30 cycles of 10 s at 98 °C, 15 s at 58 °C, and 30 s at 72 °C, and finally 5 min at 72 °C. Primer pairs are listed in Table S1 in Appendix A.

2.4. Immunofluorescence

Organoids were fixed in 4% paraformaldehyde at room temperature overnight. Phosphate-buffered saline (PBS) washed three times for 5 min each time. Dehydration in 30% sucrose, followed by optimal cutting temperature compound embedding and cryosection at 10 μm. PBS washed three times for 5 min each time. The cells were blocked with bovine serum albumin (BSA) for 30 min.

Added the first antibody and incubated at 4 °C overnight and PBS washed three times for 5 min each time. First antibodies used: SRY-box transcription factor 2 (SOX2; mouse, 1:200; GB14149; Servicebio, China), paired box 6 (PAX6; rabbit, 1:300; ab5790; Abcam, USA), neuron-specific class III β-tubulin (TUJ1; mouse, 1:500; GB15139; Servicebio), SOX2 (rabbit, 1:500; GB11249; Servicebio), NK2 homeobox 1 (NKX2.1; mouse, 1:200; GB14157; Servicebio), forkhead box protein G1 (FOXG1; mouse, 1:200; GB114738; Servicebio), calretinin (rabbit, 1:300; GB112134; Servicebio), glial fibrillary acidic protein (GFAP; mouse, 1:1000; GB12100; Servicebio), gamma-aminobutyric acid (GABA; rabbit, 1:50; ab259971; Abcam), vesicular glutamate transporter 1 (VGLUT1; rabbit, 1:500; GB11821; Servicebio).

Added secondary antibody and incubated for 50 min at room temperature away from light and PBS washed three times for 5 min each time. Alexa Fluor® 488 goat anti-rabbit Immunoglobulin G (IgG; 1:400; GB25303; Servicebio), Cy3 goat anti-mouse IgG (1:300; GB21301; Servicebio), Alexa Fluor® 488 goat anti-mouse IgG (1:400; GB25301; Servicebio), Cy3 goat anti-rabbit IgG (1:300; GB21303; Servicebio).

Added 4′,6-diamidino-2-phenylindole (DAPI; G1012; Servicebio) to re-stain the cell nuclei and incubated for 10 min at room temperature away from light. PBS washed three times for 5 min

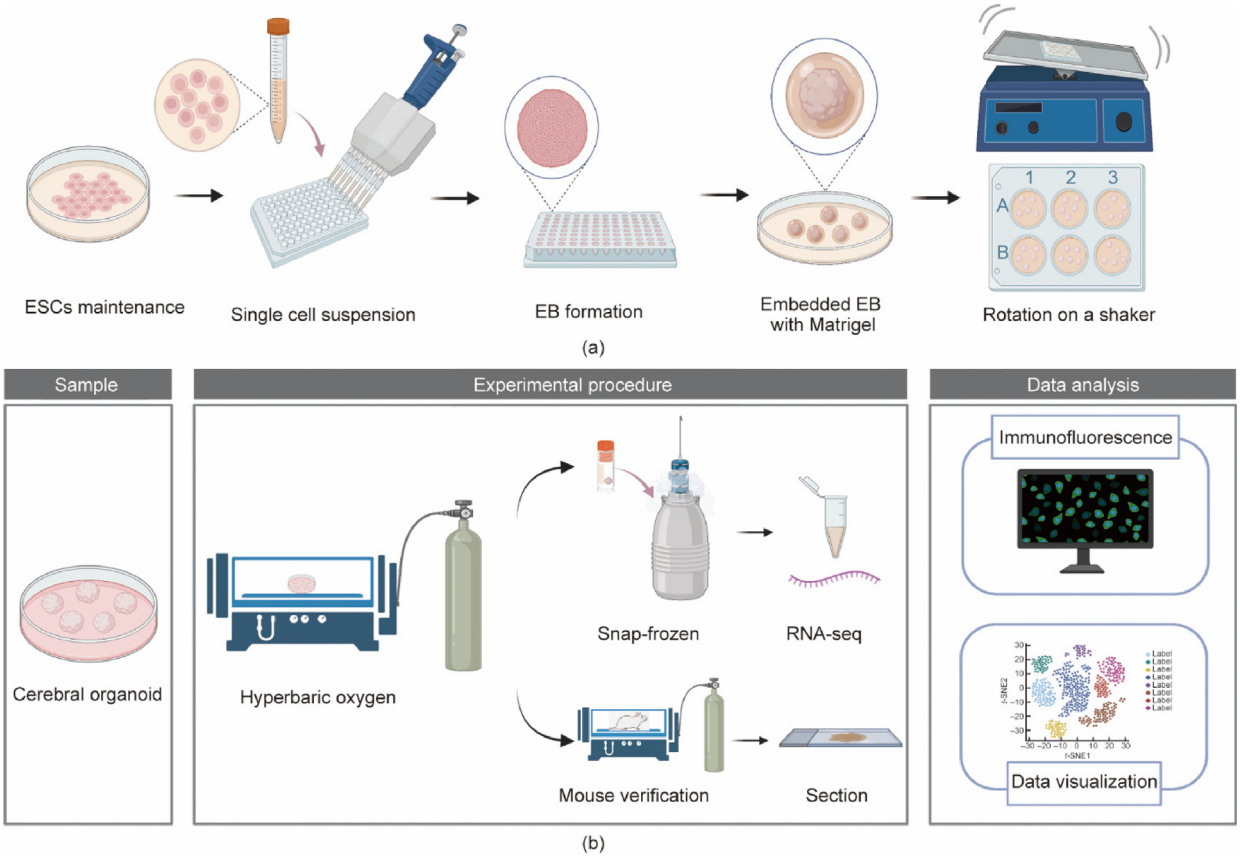

Fig. 1. Experimental design of the study of oxygen toxicity in cerebral organoids. (a) Schematic of the human cerebral organoid culture protocol. (b) Establishment and analytical pipeline of the HBO-induced CNS-OT model. ESC: embryonic stem cell; EB: embryoid body; RNA-seq: RNA sequencing.

each time. The slides were sealed with an anti-fluorescence quenching sealer.

2.5. HBO treatment

Cerebral organoids continuously exposed to five or six ATA and 95% oxygen for 60 or 120 min to establish a model of HBO toxicity. The specific treatment conditions were as follows: G1: five ATA for 60 min, G2: five ATA for 120 min, G3: six ATA for 60 min, and G4: six ATA for 120 min. The control group was the condition of normal organoid culture.

2.6. Bulk RNA sequencing (RNA-seq) and bioinformatics analysis

Each group had three replicates. Eukaryotic mRNA sequencing is based on Illumina Novaseq 6000 sequencing platform (Illumina, USA). For sequencing experiments, Illumina TruseqTM RNA sample prep Kit method was used for library construction. Total RNA was extracted, and the concentration and purity of the extracted RNA were detected by Nanodrop2000 (Thermo Fisher Scientific, USA). RNA integrity was determined by agarose gel electrophoresis, and RNA integrity number values were determined by Agilent2100 (USA). Single library construction requirement: total RNA $\geq$ 1 ug, concentration $\geq$ 35 ng·μL^{-1}, the ratio of absorbances at 260 nm and 280 nm ($OD_{260/280} \geq 1.8$; a measure of protein contamination), the ratio of absorbances at 260 nm and 230 nm ($OD_{260/230} \geq 1.0$; a measure of contamination by salts, ethylenediaminetetraacetic acid (EDTA), or organic compounds). Using magnetic beads with oligo deoxythymidine (Oligo (dT)) for A–T base pairing with ploy A, mRNA could be isolated from total RNA for analysis of transcriptome information. By adding fragmentation buffer, mRNA could be randomly broken and small fragments of about 300 bp could be isolated by magnetic bead screening. Under the action of reverse transcriptase, six-base random hexamers were added to reverse the synthesis of single-stranded RNA using mRNA as a template, followed by second-strand synthesis to form a stable double-stranded structure. The double-stranded cDNA was structured with sticky ends, which were made flat by adding end repair mix, followed by the addition of an "A" base at the 3′ end, which was used to join the Y-junction. Sequencing on the Illumina platform (PE libraries with a read length of 2 × 150 bp).

Transcriptomic data analysis included quality control, genome annotation, quantification, differential gene expression analysis, and gene set enrichment. Raw sequencing data were quality-controlled using fastp (v0.19.5) to remove reads that were too long, too short, contained excessive N bases, or exhibited low 3′ end quality. Filtered data were then evaluated with FastQC to assess sequencing quality based on Q30 scores, GC content distribution, base balance, and non-duplicate rates. Cleaned reads were aligned to the Homo sapiens reference genome GRCh38.p14 (NCBI) using STAR (v2.7.1a), and gene quantification was performed with the GENCODE v42 annotation file to generate a gene count matrix. Differential expression analysis was conducted using DESeq2 (v1.24.0) with a threshold of Benjamini–Hochberg correction (p_{adj}) < 0.001 and $|\log_2(\text{fold change (FC)})| > 1$ to identify significantly differentially expressed genes between groups. Over-representation analysis (ORA) was applied to these genes for Gene Ontology (GO) enrichment using Blast2GO (v2.5) and Kyoto Encyclopedia of Genes and Genomes (KEGG) pathway analysis using the KEGG pathway database (v2022.10), with a significance threshold of $p_{adj} < 0.05$ for enriched terms.

2.7. Validation experimentation

2.7.1. Mouse husbandry and experimentation

All experiments used 7–8-week-old, male C57BL/6J mice (~25 g). Mice were housed in isolated cages and acclimatized to our housing facility for one week before experiments. All studies with mice were approved by the Animal Care and Use Committee, Naval Medical Center, China (ethics number: NMC-202009).

Temsirolimus powder (60 mg; HY-50910; MCE, USA) was dissolved in a mixture consisting of 600 μL of absolute ethanol, 2400 μL of polyethylene glycol (PEG) 300, 300 μL of Tween-80, and 2700 μL of saline to achieve a final concentration of 10 mg·mL^{-1}. The resulting formulation comprised 10% absolute ethanol, 40% PEG 300, 5% Tween-80, and 45% saline by volume. A volume of 0.25 mL of the formulation was administered to each mouse (approximately 25 g body weight), resulting in a total dosage of 100 mg·kg^{-1}.

Mice were divided into four groups with 6 8 mice in each group. Control group: Each mouse was intraperitoneally injected with 0.25 mL of solvent without temsirolimus; HBO group: Each mouse was intraperitoneally injected with 0.25 mL of solvent 1 h before exposure, and then continuously exposed to an environment of six ATA and 95% oxygen for 60 min; Temsirolimus group: Each mouse was intraperitoneally injected with 0.25 mL of temsirolimus solution; HBO + temsirolimus intervention group: Each mouse was intraperitoneally injected with 0.25 mL of temsirolimus solution 1 h before exposure, and then continuously exposed to an environment of six ATA and 95% oxygen for 60 min. The mice in the HBO group and HBO + temsirolimus group were exposed to hyperbaric oxygen, while the control group and temsirolimus group were exposed to an air environment, and all treatment times were 60 min.

2.7.2. RT-qPCR

The expression levels of mammalian target of rapamycin (mTOR) pathway-related genes (serine/threonine kinase (*AKT*), AMP-activated protein kinase catalytic subunit alpha 1 (*AMPKα1*), AMP-activated protein kinase catalytic subunit alpha 2 (*AMPKα2*), tuberous sclerosis complex 1 (*TSC1*), tuberous sclerosis complex 2 (*TSC2*), *mTOR*, and mTOR complex 1 (*mTORC1*)) were analyzed. The procedure was the same as in Section 2.3, with primers listed in Table S1.

2.7.3. Immunohistochemistry/immunofluorescence

After HBO treatment, the mice were anesthetized in an air anesthesia machine (RWD, China). After initial internal fixation by perfusion with 4% paraformaldehyde from the left heart, whole brain tissues were removed and fixed overnight in 4% paraformaldehyde. Dehydrated, embedded in paraffin, and sectioned. After deparaffinized and rehydrated, added first antibody and incubated overnight at 4 °C. Added second antibody conjugated with horseradish peroxidase (HRP) at room temperature for 50 min. Added the tyramide signal amplification (TSA) reagent and incubated for 10 min. Added DAPI for 10 min, and then observed under a fluorescence microscope.

The 8-hydroxy-2′-deoxyguanosine (8-OHdG) immunofluorescence staining was the same as in Section 2.4.

Antibodies used: c-Fos (1:1000; ab190289; Abcam), mTOR (1:4000; GB111839; Servicebio), 8-OHdG (1:300; HY-P81140; MCE), goat anti-rabbit IgG conjugated with HRP (1:500; GB23303; Servicebio), goat anti-mouse IgG conjugated with HRP (1:500; GB23301; Servicebio), CY3-tyramide (CY3-TSA; G1223; Servicebio), iF647-TSA (G1232; Servicebio), FITC-TSA (G1222; Servicebio), goat anti-rabbit IgG (1:400; GB25303; Servicebio).

2.7.4. Quantitative fluorescence analysis

Quantitative analysis was performed using ImageJ. All images were acquired under identical microscope settings, uniformly converted to 8-bit grayscale, and background-corrected. The c-Fos$^+$ cell ratio was calculated as the integrated density of c-Fos signals normalized to the measured area (IntDen/Area).

2.8. Statistical analysis

SPSS 19 was used for statistical analysis. The Shapiro–Wilk test and Levene's test were applied to assess normality and homogeneity of variances, respectively. On this basis, unpaired *t*-tests were used for pairwise comparisons between two groups; for comparisons among multiple groups, one-way analysis of variance (ANOVA) was first performed, and if statistically significant differences were observed, pairwise comparisons between groups were then conducted using the Tukey method. $P < 0.05$ was applied for all statistical tests to determine statistically significant differences.

3. Results and discussion

3.1. Modeling neural development with cerebral organoids

To investigate the effects of HBOT on the human nervous system, we generated cerebral organoids from validated hESCs expressing pluripotency markers (octamer-binding transcription factor 4 (OCT4), stage-specific embryonic antigen 4 (SSEA4), T-cell leukemia/lymphoma-related antigen 1-60 (TRA-1-60), and SOX2; Fig. S1 in Appendix A). Following an established differentiation protocol [18,22], the organoids exhibited characteristic neural development patterns (Figs. 2(a) and (b)).

During differentiation, we observed the expected molecular transitions: the expression of pluripotency markers (OCT4 and Nanog) decreased whereas that of neural progenitor markers (SOX1 and PAX6) increased, confirming successful neural induction (Figs. 2(c) and (d)). Neural rosette structures formed by day 20 (Fig. 2(e)), and with continued culture, they produced expanded neuroepithelial tissues showing progressive structural complexity (Fig. 2(e), Fig. S2 in Appendix A).

Immunofluorescence analysis validated the spatiotemporal distribution patterns of specific cell types. On day 20, the expression of the neural progenitor markers SOX2 and PAX6 was robust (Fig. 3(a)), while the neurons remained sparsely distributed. By day 40, the cortical plate marker T-box brain transcription factor 1 (TBR1) and early-born neuronal marker chicken ovalbumin upstream promoter transcription factor-interacting protein 2 (CTIP2) were predominantly localized to peripheral regions, with the immature neuronal marker TUJ1 concentrated in inner zones (Figs. 3(b) and (c)). This spatial organization recapitulates the characteristic layered structure of the developing mammalian neocortex, where newborn neurons generated in ventricular zones undergo inside-out radial migration along glial fibers [23].

Notably, TUJ1$^+$ cell numbers increased significantly during this stage, with a characteristic perisomatic distribution around SOX2$^+$ cells (Fig. 3(c)). These findings confirm the developmental sequence of neuronal production via asymmetric progenitor division followed by radial migration. Although most neurons remain immature, these patterns demonstrate ongoing neurogenic progression.

During organoid development, forebrain regions exhibited preferential maturation, as evidenced by robust expression of the forebrain-specific marker FOXG1 (Fig. 3(d)). Regional identity specification was further confirmed by immunostaining for markers of the hippocampus (neuropilin 2 (NRP2)), ventral forebrain

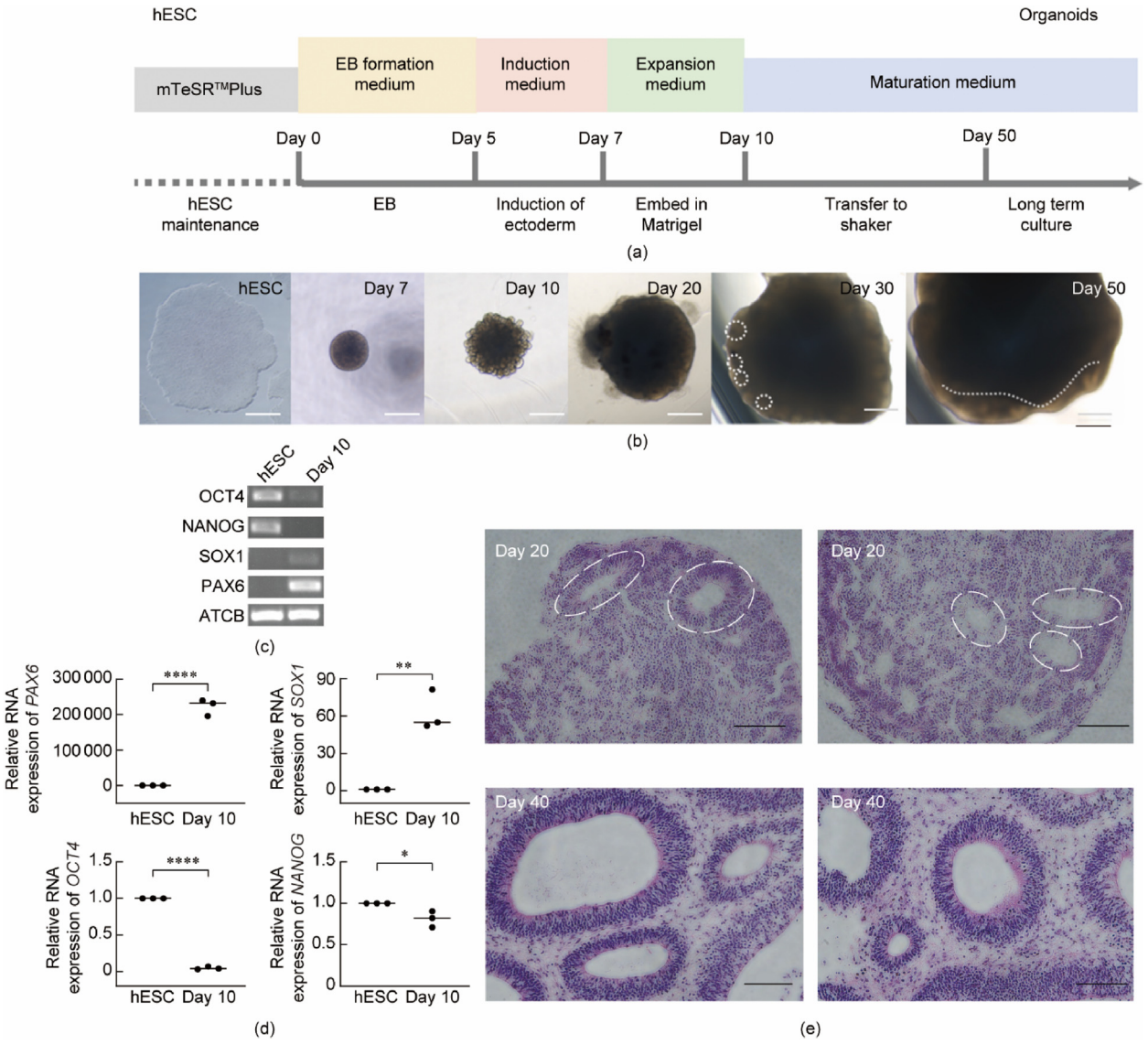

Fig. 2. Generation and characterization of human cerebral organoids. (a) Schematic of cerebral organoid differentiation from hESCs. (b) Bright-field images showing organoid morphology at successive developmental stages. (c) Gel electrophoresis analysis of pluripotency (OCT4, NANOG) and neural progenitor (SOX1, PAX6) markers. (d) Expression of genes (*OCT4*, *NANOG*, *SOX1*, and *PAX6*). (e) Hematoxylin and eosin (H&E)-stained sections demonstrating organoid cytoarchitecture at days 20 and 40. Scale bars: 500 μm.

(NKX2.1), and dorsal forebrain (PAX6) (Figs. 3(e) and (f)), demonstrating the establishment of distinct brain regions identities with complex tissue organization and characteristic epithelial morphologies.

Functional characterization revealed established synaptic networks in which excitatory ($VGLUT1^+$) and inhibitory (gamma-aminobutyric acid transporter 1 ($GAT1)^+$) neuronal populations were coexpressed (Fig. 3(g)). These neurons formed intricate local circuits within peripheral organoid regions, demonstrating electrophysiologically competent connectivity. The neural microenvironment contained $GFAP^+$ cells interspersed among neuronal layers (Fig. 3(h)), comprising primarily astrocytes while potentially retaining radial glial or neural progenitor populations, collectively fulfilling essential trophic and structural support functions [24].

Additionally, we investigated the effects of the initial cell number on the morphology and development of cerebral organoids. During early development, the seeding density of EBs significantly influenced organoid diameter (Fig. S3 in Appendix A). After ten days of culture, the intergroup differences gradually diminished, whereas the intragroup variability became more pronounced. Therefore, we selectively used tissues of similar size from the same batch for subsequent experiments. Although the initial cell number did not affect the final size of the mature organoids, it influenced the differentiation of the germ layer within the EBs. In general, lower numbers of cells yielding smaller EBs resulted in a greater degree of ectodermal commitment, whereas higher numbers of cells producing larger EBs resulted in the generation of more active and diverse neural tissues (Figs. S4 and S5 in Appendix A). On the basis of these observations, an initial seeding density of 9000 cells per well was selected for all further experiments.

Transcriptomic sequencing revealed that cerebral organoids from 20 to 70 d exhibited relatively stable transcription, with samples from the same time period clustering well (Fig. S6 in Appendix A). In the principal component analysis (PCA), samples within 30 d and those beyond 30 d were clearly separated along the first principal component (PC1; contributing 38.8% of the variance), whereas 50 d samples on the PC2 axis were further distinguished from 60 to 70 d samples (9.4% contribution). These results suggest that cerebral organoids cultured for more than 30 d may display a greater degree of maturity at the transcriptional level. Previous

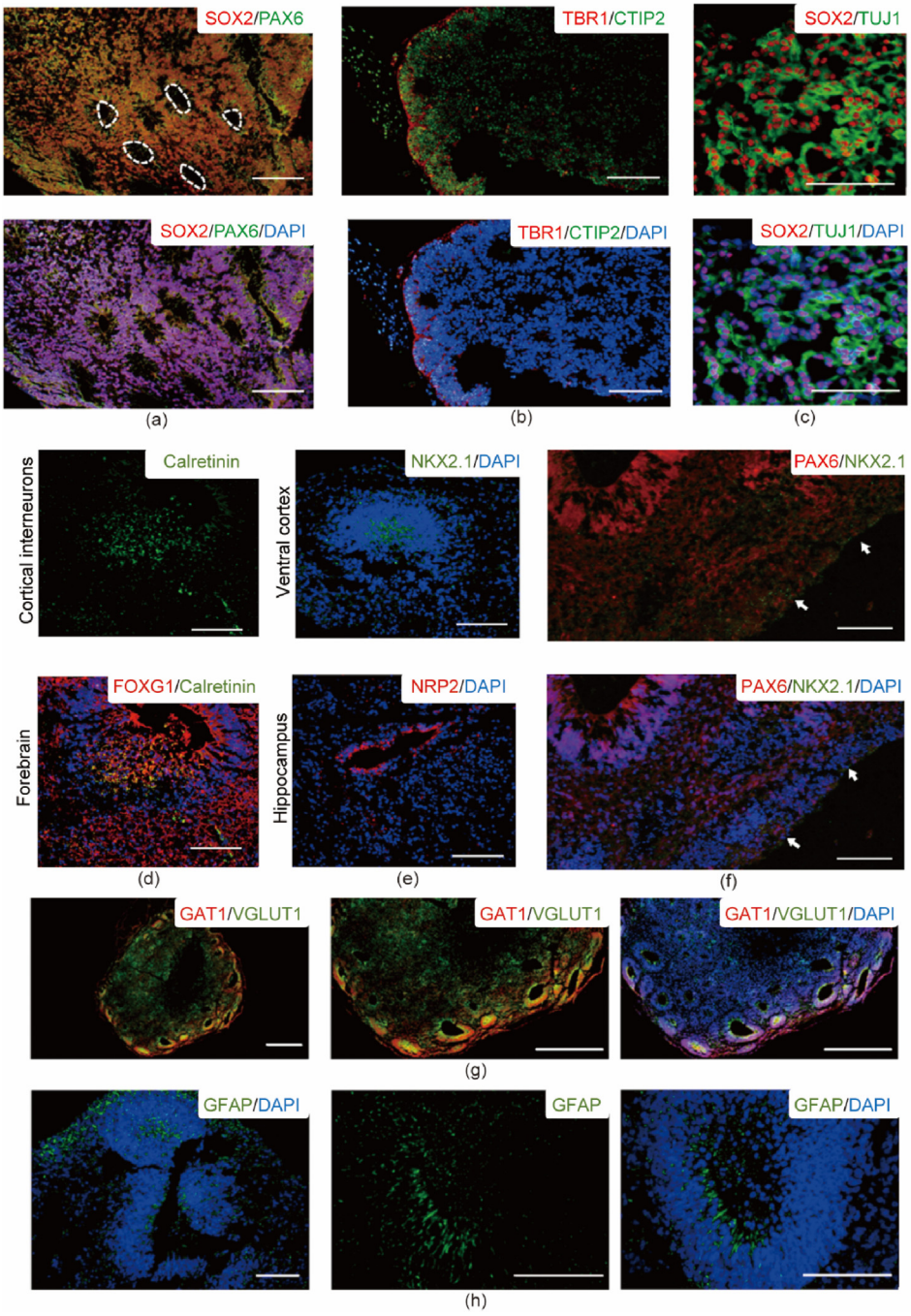

Fig. 3. Human cerebral organoids recapitulate the identities of various brain regions. (a) Neural progenitors (SOX2, red; PAX6, green). (b) Cortical plate marker (TBR1, red) and early-born neurons (CTIP2, green). (c) Neural progenitors (SOX2, red) and immature neurons (TUJ1, green). (d) Forebrain markers (FOXG1, red) and cortical interneurons (calretinin, green). (e) Ventral forebrain (NKX2.1, green) and hippocampus (NRP2, red). (f) Dorsal forebrain (PAX6, red) and ventral forebrain (NKX2.1, green). (g) GABAergic neurons (GABA, red) and glutamatergic neurons (VGLUT1, green). (h) Astrocytes (GFAP, green). Scale bars, 100 μm (a–f) and 500 μm (g, h).

studies have also confirmed that cerebral organoids exhibit greater cellular diversity beyond 33 d of development. Moreover, compared with those cultured for 33–37 d, organoids at 41–65 d express nearly all genes found in fetal cortical cells, closely resembling the transcriptional profile of the human brain at 16–18 weeks of gestation [25].

The cerebral organoid model established in this study faithfully recapitulates key features of early fetal brain development, including complete neurogenic progression, cortical lamination, functional neuronal differentiation, and stable transcriptional profiles. Extended cultivation could further promote the generation of mature neuronal populations, thereby providing a more sophisticated *in vitro* platform for investigating human brain development.

3.2. Effects of acute HBO exposure on the transcriptome of cerebral organoids

To systematically investigate HBO-mediated neurotoxicity, we established four acute exposure paradigms simulating diving/therapeutic conditions (G1: five ATA for 60 min, G2: five ATA for 120 min, G3: six ATA for 60 min, and G4: six ATA for 120 min). Comparative transcriptomic profiling was performed against

normoxic controls to identify genes associated with CNS oxygen toxicity.

All sequencing data demonstrated high-quality metrics (where Q20 and Q30 denote Phred quality scores of ≥ 20 and ≥ 30, respectively), with > 6.01 GB of clean data, a Q30 base ratio > 93.88%, a Q20 base ratio > 97.73%, and an error rate < 0.0253% (Figs. S7(a)–(c) in Appendix A). The average GC content was 49.23%, with 48 832 341 raw reads and 48 216 589 clean reads, yielding a clean ratio of 98.68% (Figs. S7(d)–(f) in Appendix A). Additionally, the sequencing coverage distribution was uniform without significant bias (Fig. S8 in Appendix A). Alignment against the reference genome GRCh38 produced an average of 48 216 589 total reads, with 96.60% total mapped reads, 93.13% uniquely mapped reads, and 3.47% multiple mapped reads (Figs. S9 and S10 in Appendix A). Overall, the alignment efficiency was highly satisfactory, with no evidence of sample contamination.

Younger organoids (< 30 d) exhibited minimal HBO sensitivity (Fig. S11 in Appendix A), with PCA primarily reflecting developmental timelines, which is consistent with reported resistance in immature rodents (≤ 20 d) [26,27]. Further evidence suggests that this protection stems from underdeveloped neural networks rather than blood–brain barrier immaturity or the inability to generate seizures [26,28,29]. With respect to cerebral organoids, those cultured for 41–67 d exhibit a more comprehensive transcriptional profile [25]. Therefore, subsequent experiments utilized organoid samples cultured for 50–70 d, which corresponds to the late first to second trimester stages of fetal development.

Transcriptomic profiling revealed that oxygen partial pressure was the dominant factor influencing gene expression patterns in the organoids at 50–70 d, with the developmental stage contributing minimally to transcriptional variation. PCA demonstrated complete segregation of the five ATA (groups G1/G2) and six ATA (groups G3/G4) groups along PC1 (Fig. 4(a)). The robust pressure-dependent clustering pattern persisted in pairwise comparisons (G1/G2 and G1/G3 groups), confirming that acute hyperbaric pressure overrides developmental transcriptional programs in maturing neural tissue.

Comparative analysis revealed 10 415, 10 427, 5335, and 5573 differentially expressed genes (DEGs) in groups G1–G4, respectively, relative to those in the controls. Among these, 2717 DEGs (12.35% of the total) were common to all four treatment groups (Figs. 4(b) and (c)). Although the total number of genes detected was similar across groups, the notably lower number of DEGs in groups G3 and G4 may be attributed to their higher expression stability, resulting in fewer genes meeting the significance threshold ($|\log_2 FC| \geq 1$, $p_{adj} < 0.001$; Fig. S12 in Appendix A). Demchenko et al. [30] reported that short-term or low-pressure hyperbaric oxygen exposure affected cerebral blood flow in mice, but when the oxygen partial pressure reached five ATA after 45 min of exposure, cerebral blood flow returned to preexposure levels. These findings suggest that stronger or longer-lasting stimuli may activate intrinsic regulatory mechanisms more rapidly. Further analysis is needed to clarify the specific biological implications and regulatory mechanisms underlying these shared and group-specific DEGs. Similarly, cluster analysis of expression patterns revealed two distinct profiles that were primarily segregated by oxygen partial pressure rather than exposure duration (Fig. 4(d)). On the basis of these findings, subsequent analyses focused specifically on pressure-dependent effects.

3.3. HBO-induced CNS-OT mechanisms in cerebral organoids

HBO exposure induces distinct pressure-dependent responses in cerebral organoids, mediated through coordinated multipathway regulatory networks. GO and KEGG enrichment analyses of organoids exposed to five ATA and six ATA of HBO revealed differential stress response patterns under varying pressure conditions. Specifically, five ATA exposure predominantly disrupted neurotransmitter transport and elicited early stress responses, characterized by significant activation of glutamatergic synapse pathways, synaptic vesicle cycling, and p53 signaling (Figs. 5(a) and (b)). These findings were corroborated by RT-qPCR, which revealed marked upregulation of key genes (glutamate-ammonia ligase (*GLUL*), glutamate ionotropic receptor alpha-amino-3-hydroxy-5-methyl-4-isooxazole-propionic acid type subunit 3 (*GRIA3*), and metabotropic glutamate receptor 3 (*GRM3*)) (Fig. 5(c)).

These alterations may be closely associated with oxidative stress-mediated lysosomal dysfunction, in which reactive oxygen species (ROS) induce lipid peroxidation of the lysosomal membrane, subsequently compromising its stability and disrupting lysosomal membrane permeabilization [31]. Lysosomal destabilization not only disrupts the acidic lumen and hydrolase activity but, more critically, interferes with the signaling platform on the lysosomal surface, thereby affecting the activity of the mTORC1 pathway. Studies have demonstrated that the lysosome serves as the central site for mTORC1 activation, and that its functional status directly regulates the localization and activity of mTORC1 [32,33]. Signals such as amino acids mediate the recruitment and activation of mTORC1 via vacuolar H^+-adenosine triphosphatases (ATPase) and Rag guanosine triphosphatase (GTPase) complexes [34]. Disruption of lysosomal membrane integrity is likely to interfere directly with this precisely regulated mechanism [34].

Notably, the marked activation of the p53 signaling pathway suggests the triggering of DNA damage response mechanisms [35], although under these pressure conditions, it primarily manifests as cell cycle arrest and repair responses. This observation is further supported by the transcriptional changes in specific genes. Genes associated with antioxidant activity (such as glutathione-disulfide reductase (*GSR*), peroxiredoxin 1 (*PRDX1*), and *PRDX2*), cell cycle arrest (including cyclin-dependent kinase 2 (*CDK2*), *CDK4*, E2F transcription factor 1 (*E2F1*), and WEE1 G2 checkpoint kinase (*WEE1*)), and mitochondrial function (e.g., succinate dehydrogenase complex subunit C (*SDHC*) and ubiquinol-cytochrome *C* reductase core protein 1 (*UQCRC1*)) exhibited more active transcription in groups G1 and G2 (Figs. S13–S17 in Appendix A). In contrast, the changes in the expression of these genes in groups G3 and G4 were not significant compared with those in the control group, indicating that cells can still initiate adaptive stress responses under lower-pressure conditions.

When the pressure was increased to six ATA, the neural injury pattern underwent a significant transition, entering a new phase characterized by altered synaptic plasticity and dysregulation of the dopaminergic system. Transcriptomic analysis revealed specific activation of long-term potentiation (LTP) and dopaminergic synapse pathways (Figs. 5(d) and (e)), with RT-qPCR confirming the upregulated expression of key genes, including tyrosine hydroxylase (*TH*; Fig. 5(f)). Notably, while cell cycle and cellular senescence pathways were enriched under both pressure conditions, distinct apoptotic signatures emerged exclusively at six ATA, suggesting a threshold effect in which HBO-induced cellular damage shifts from reversible stress to irreversible cell death. Under these elevated pressure conditions, the p53 signaling network exhibited a functional switch toward promoting apoptosis, demonstrating its pressure-dependent regulatory plasticity.

At the molecular level, pathway enrichment analysis revealed multiple enzyme-related pathways, highlighting the central role of the lysosome–oxidative stress axis in HBO-induced injury. Oxidative stress-induced lysosomal membrane permeabilization not only leads to the leakage of hydrolases that directly activate cell death execution molecules but also may disrupt lysosome-dependent mTORC1 signal transduction, thereby affecting autophagic flux and cellular metabolic homeostasis and ultimately

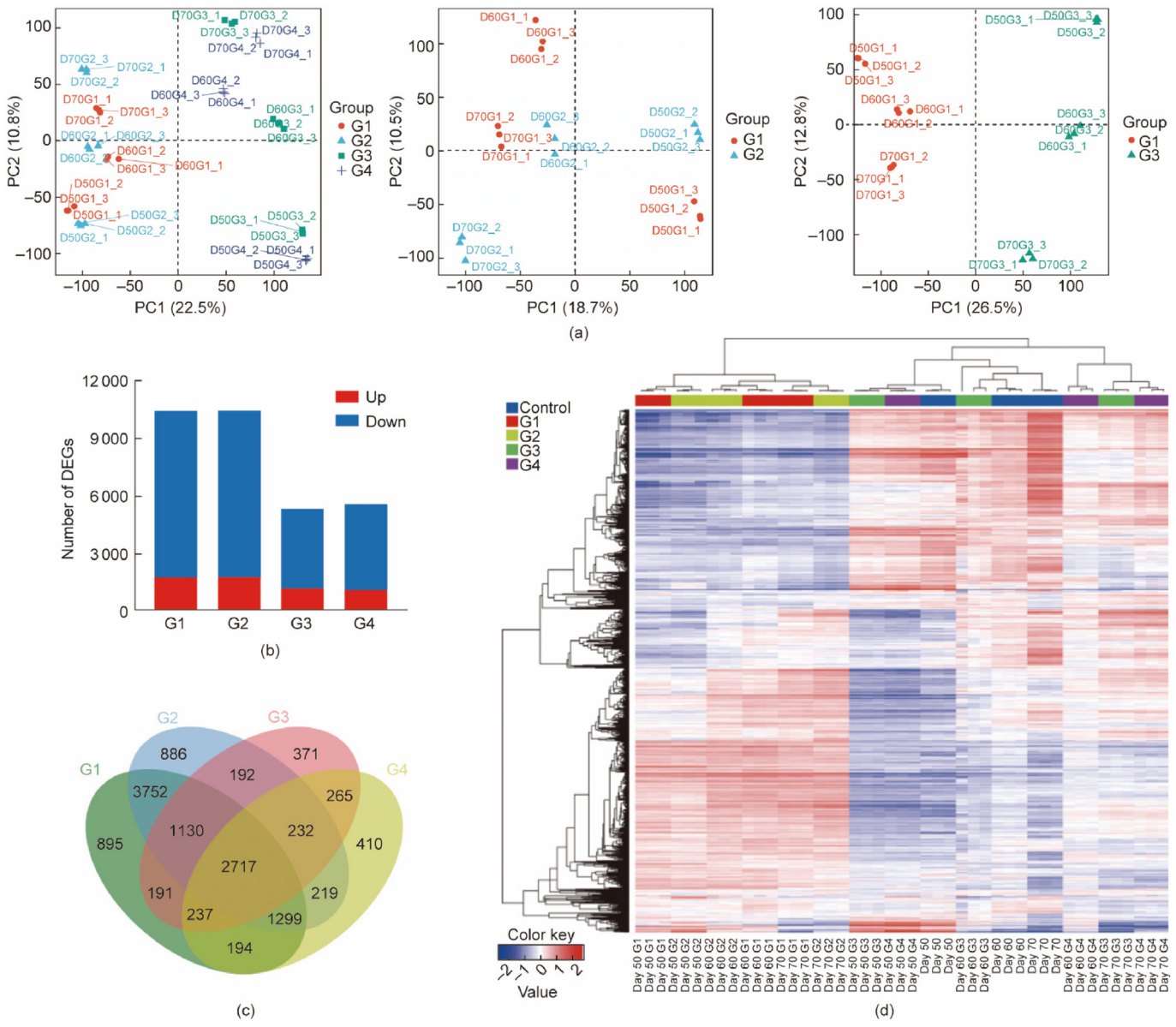

Fig. 4. Transcriptional changes in cerebral organoids following acute HBO exposure. (a) PCA. (b) DEGs under different treatment conditions versus the control. (c) Venn diagram of coexpressed DEGs. (d) Heatmap of gene expression in different treatment groups.

determining cell fate [36–38]. In this context, the sustained activation of the p53 signaling network plays dual roles under different pressure conditions: at five ATA, p53 signaling likely favors cell cycle arrest and the promotion of repair mechanisms to maintain genomic stability whereas under severe stress at six ATA, irreversible damage caused by lysosomal disintegration and aberrant mTOR activation may shift p53 signaling toward a pro-apoptotic state. This pressure-dependent switch in p53-mediated outcomes is likely finely regulated upstream by lysosomal status and mTOR signaling dynamics, warranting further investigation.

To further verify that these changes were induced by the HBO environment rather than the intrinsic heterogeneity of the cerebral organoids, differential gene expression analysis using Deseq2 and GO/KEGG enrichment analysis were also performed on the control group. When only samples from days 50–70 were analyzed and the same filtering criteria ($|\log_2 FC| \geq 1$ and $p_{adj} < 0.001$) used for the treatment group were applied, no DEGs were identified (Fig. S18 in Appendix A). Therefore, samples from days 20–30 were included to comprehensively analyze transcriptional changes during development. The results revealed that variations in culture duration led to alterations in pathways related to enzymatic activity and synaptic function, which may be associated with neuronal maturation and synaptic transmission during development (Fig. S19 in Appendix A). Notably, the results of the GO enrichment analysis highlighted the "response to light stimulus" pathway, with upregulated expression of related genes over longer culture periods. These findings suggest that extended culture may promote the maturation of neural circuits, increasing sensitivity to light variations in the environment [39]. KEGG analysis revealed that the most significantly enriched pathways were the phosphoinositide 3-kinase (PI3K)–AKT, cyclic adenosine monophosphate (cAMP), and cyclic guanosine monophosphate (cGMP)–cGMP-dependent protein kinase (PKG) signaling pathways, indicating that these pathways are influenced by the culture time. Although these pathways were not significantly enriched in the days 50–70 analysis, subsequent studies should consider whether changes in these pathways are more strongly affected by the culture duration than by the HBO environment.

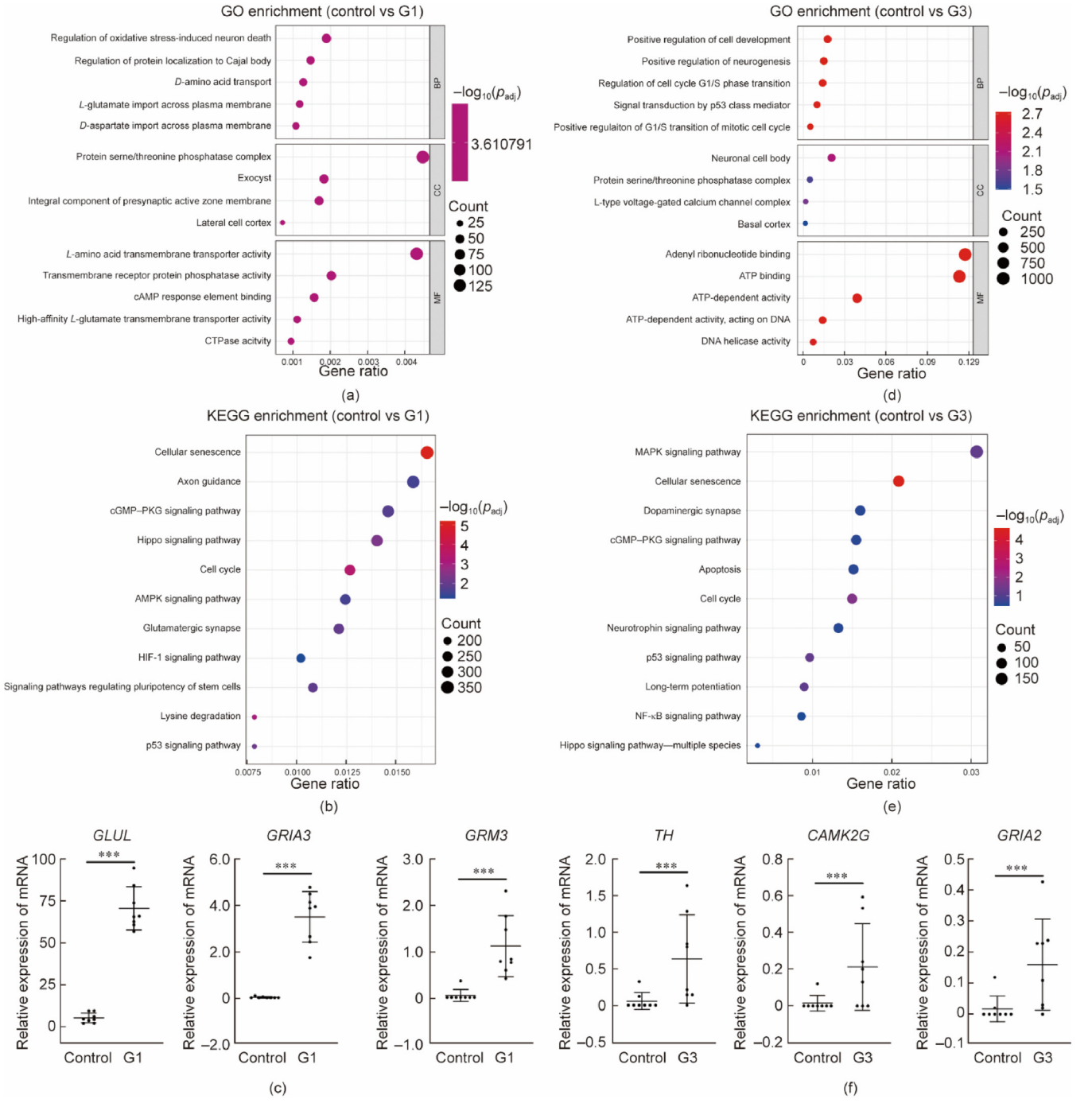

Fig. 5. (a) GO and (b) KEGG analyses of organoids exposed to HBO for 60 min. (c) Expression of glutamate and receptor-related genes. (d) GO and (e) KEGG analyses of organoids exposed to HBO for 120 min. (f) Expression of LTP- and dopaminergic synapse-related genes. ***$P < 0.001$. cAMP: cyclic adenosine monophosphate; CTPase: C-terminal processing proteases; cGMP: cyclic guanosine monophosphate; PKG: cGMP-dependent protein kinase; AMPK: adenosine monophosphate-activated protein kinase; HIF-1: hypoxia-inducible factor-1; NF-κB: nuclear factor κB.

Furthermore, the p53 pathway was not enriched at any culture stage, supporting the conclusion that its alterations are specifically induced by HBO. For the apoptosis pathway identified in KEGG, a detailed analysis of significantly differentially expressed genes was conducted to determine during which culture periods these changes occurred. As shown in Fig. S20 in Appendix A, pro-apoptotic and anti-apoptotic genes such as B-cell lymphoma 2-like 2 (*BCL2L2*), baculoviral IAP repeat containing 5 (*BIRC5*), caspase 3 (*CASP3*), and *CASP6* were generally highly expressed from days 20–30 but were expressed at lower levels from days 50–70. After HBO exposure, the expression of pro-apoptotic genes, including BCL2 associated agonist of cell death (*BAD*), BH3 interacting domain death agonist (*BID*), *CASP3*, and *CASP9*, did not significantly change, whereas the expression of anti-apoptotic genes, such as myeloid cell leukemia 1 apoptosis regulator (*MCL1*), *BCL2L2*, and B-cell lymphoma 2 (*BCL2*), was upregulated in the G1 and G2 samples (Fig. S21 in Appendix A). This upregulation of antiapoptotic genes may mitigate HBO-induced damage, explaining why exposure to five ATA did not lead to significant changes in apoptosis.

3.4. HBO-induced pathway dysregulation in cerebral organoids

Transcriptomic profiling of cerebral organoids under differential HBO pressures (five ATA vs six ATA) demonstrated pressure-graded neurotoxicity. Notably, although the differential expression of individual genes was less pronounced under the six ATA condition than under the five ATA condition, both the GO and KEGG enrichment analyses revealed a greater gene ratio in the six ATA group. This suggests that exposure to higher pressure elicits a more coordinated transcriptomic regulatory response, resulting in broader pathway-level adaptations. In contrast, under the relatively moderate stress of five ATA, the organoids responded through strong upregulation or downregulation of a limited set of critical genes. The results of mouse experiments confirmed that short-term, mild HBO exposure ($\leq$ five ATA, $\leq$ 30 min) can lead to a reduction in cerebral blood flow, whereas prolonged and high-intensity exposure ($\geq$ five ATA, $\geq$ 45 min) may restore blood flow regulation to normal levels [40,41]. However, this "normal level" state was unstable and rapidly increased to 160% of baseline. The regulatory mechanisms triggered by such high-intensity stimuli warrant further investigation. On the basis of these findings, further investigation into pathway-level alterations under six ATA conditions is warranted.

Exposure to six ATA in HBO specifically activated multiple critical signaling pathways, including the mTOR, AMPK, and PI3K–AKT pathways (Figs. S22–S24 in Appendix A). Aberrant activation of the mTOR signaling pathway is particularly prominent and is closely correlated with clinically observed seizure activity following oxygen toxicity [42]. As a key downstream effector of both the PI3K–AKT and AMPK signaling cascades, mTOR integrates diverse environmental stimuli through its complexes (mTORC1 and mTORC2) to regulate neuronal growth, metabolism, and plasticity [43].

This study revealed that hyperbaric oxygen exposure downregulates mouse protein 25 (MO25) expression, leading to aberrant AMPK activation (Fig. S23). Activated AMPK regulates mTORC1 activity through the following dual mechanisms: ① direct inhibition of mTORC1 phosphorylation and ② indirect modulation through the promotion of TSC1/2 complex phosphorylation [44,45]. This regulatory pattern aligns with established reports on the crucial role of TSC1/2 in mediating mTORC1 responses to oxidative stress [46]. Notably, as a key negative regulator of the mTOR pathway, TSC1/2 expression is coordinately controlled by multiple signaling pathways, including AMPK, TNF, MAPK and Wnt [47,48]. This intricate network-level regulation may underlie the neuronal dysfunction observed following hyperbaric oxygen exposure.

From a signal transduction perspective, the PI3K–AKT–mTOR axis plays a pivotal role in mediating hyperbaric oxygen-induced neurotoxicity. Our study demonstrated that HBO exposure activates the PI3K–AKT pathway, leading to direct AKT-mediated mTOR phosphorylation, which subsequently dysregulates fundamental cellular processes, including cell cycle progression, proliferation, and differentiation [49]. These findings provide novel mechanistic insights into HBO-induced neurological damage.

Changes in the expression of genes associated with the mTOR pathway revealed that mTOR-related gene expression remained relatively stable in the control group (days 50–70; Fig. S25 in Appendix A). However, after HBO treatment, the expression of most genes in this pathway increased to varying degrees. Specifically, *AKT1*, eukaryotic translation initiation factor 4E binding protein 2 (*EIF4EBP2*), protein kinase AMP-activated non-catalytic subunit beta 2 (*PRKAB2*), and Unc-51 like autophagy activating kinase 2 (*ULK2*) were markedly upregulated in the G1 and G2 groups, whereas *TSC2* and ras homolog enriched in brain 2 (*Rheb*) expression was slightly elevated in the G3 and G4 groups (Fig. S26 in Appendix A). These findings suggest that HBO exposure consistently perturbs mTOR signaling, although the specific regulatory mechanisms differ under varying pressure conditions. In particular, the six ATA treatments appeared to preferentially involve regulation mediated by the TSC2 complex. These results further support the notion that although more genes were altered in the six ATA group, the extent of change in certain individual genes was more pronounced in the five ATA group.

Our findings revealed distinct pressure-dependent neurotoxicity mechanisms: under five ATA HBO, neurotoxicity manifested primarily as glutamatergic system dysregulation and oxidative stress-mediated lysosomal damage, where ROS accumulation increased lysosomal membrane permeability, triggering cathepsin release and exacerbating neuronal dysfunction. In contrast, six ATA HBO exposure exceeded cellular compensatory capacity, shifting the injury pattern to mTOR pathway dysregulation-dominated alterations in synaptic plasticity. The TSC1/2–mTORC1 axis serves as a critical molecular switch in this pressure-dependent transition: lysosomal damage (via cathepsin B/D release) activated mTORC1 signaling, while mTORC1 overactivation further suppresses autophagy-lysosomal function [50], establishing a vicious cycle (Fig. 6).

Notably, a bidirectional regulatory loop exists between the lysosome–oxidative stress axis and the mTOR pathway: ROS accumulation compromises lysosomal membrane integrity, triggering abnormal mTORC1 dissociation and activation from lysosomal surfaces. Conversely, mTORC1 hyperactivation suppresses the nuclear translocation of transcription factor EB (TFEB)—the master regulator of lysosomal biogenesis—thereby impairing lysosomal regeneration capacity. This positive feedback cycle likely constitutes the core mechanism underlying the pressure-dependent exacerbation of HBO-induced neurotoxicity.

On the basis of these mechanistic insights, targeted modulation of the mTOR pathway (e.g., via rapamycin and its derivatives) not only directly suppresses mTORC1 hyperactivation but also restores TFEB-mediated lysosomal biogenesis, thereby disrupting the vicious cycle of oxidative stress–lysosomal dysfunction–mTOR overactivation [51].

3.5. Mouse experiments validation of the cerebral organoid findings

The central objective of this study was to investigate the neurotoxic effects of HBO in occupational contexts such as diving. In such scenarios, the exposed subjects are typically adults with mature physiological functions, and their neural cells—such as neurons and glia—have reached a functionally stable state. While current cerebral organoid models can mimic the nervous system up to late early-to-mid pregnancy stages, they still lack mature synaptic connectivity and sufficient tissue complexity [52].

With respect to HBO-related research, the mature mouse brain shares critical characteristics with the human brain: both stably express cell type-specific markers (e.g., neuronal nuclei (NeuN) in neurons and GFAP in astrocytes), and both rely predominantly on aerobic metabolism, where mitochondria generate ATP through oxidative phosphorylation [53]. Characteristic injury responses observed in human cerebral organoids under HBO exposure—such as elevated ROS levels and mitochondrial dysfunction—can be correlated in mature mouse models through homologous cellular damage mechanisms [54]. Therefore, we established a mouse *in vivo* model to validate the critical role of the mTOR pathway in HBO-induced neurotoxicity identified in cerebral organoid studies.

The experimental design included HBO-exposed groups and temsirolimus (mTOR inhibitor)-treated intervention groups (Fig. 7(a)). Through behavioral, molecular, and histological analyses, we systematically verified both the central involvement of mTOR signaling in HBO-mediated neural damage and the effectiveness of pharmacological intervention.

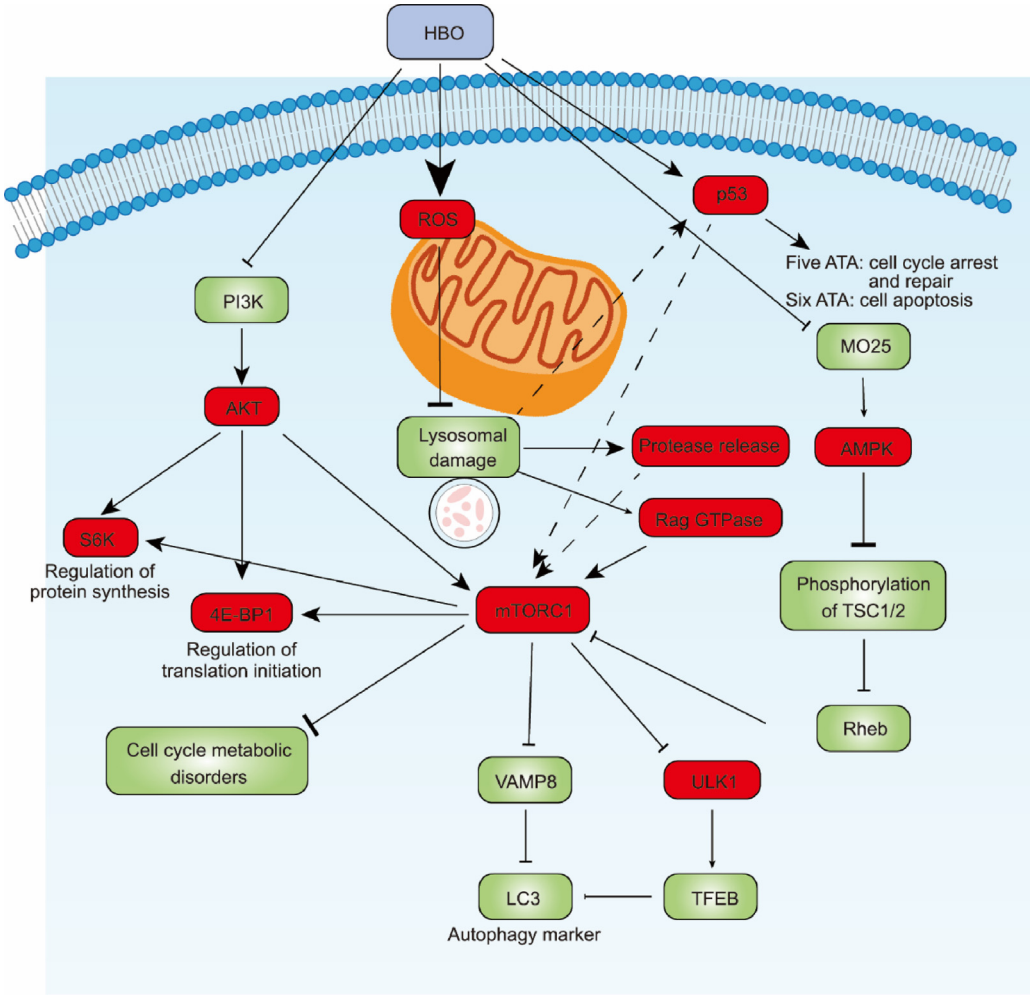

Fig. 6. Dysregulated signaling pathways induced by HBO exposure. Red: upregulated; green: downregulated. S6K: ribosomal protein S6 kinase; 4E-BP1: eukaryotic translation initiation factor 4E-binding protein 1; VAMP8: vesicle associated membrane protein 8; LC3: microtubule associated protein 1 light chain 3; ULK1: Unc-51 like autophagy activating kinase 1; TFEB: transcription factor EB.

Behavioral assessments revealed that HBO-exposed mice developed characteristic neurotoxic symptoms, including convulsions, tremors, and tonic–clonic seizures, within 10 min, with one fatal case. Notably, while temsirolimus pretreatment did not completely prevent symptom onset, it significantly reduced seizure severity. Compared with the HBO group, the intervention group maintained an upright posture significantly longer with no mortality observed. These findings strongly corroborate the neuroprotective effects of mTOR inhibition predicted by previous cerebral organoid studies.

Molecular analyses revealed the mechanism of mTOR pathway hyperactivation. While mTOR gene transcription remained unaltered, we observed significant upregulation of mTORC1 complex components and their regulators *AMPKα1* and *TSC1* (Fig. 7), perfectly recapitulating the activation pattern identified in organoid studies. Temsirolimus, a specific *mTORC1* inhibitor targeting the FRB domain, effectively blocked HBO-induced mTORC1 hyperactivation and substantially suppressed the compensatory upregulation of *AMPKα1* and *TSC1* [55].

Spatial profiling of neuronal activation via c-Fos immunostaining revealed selective regional vulnerability to HBO exposure. Prominent neuronal activation was detected exclusively in the hippocampal and temporal cortical regions, with no significant c-Fos induction observed in other brain areas (Fig. 8(a), Fig. S27 in Appendix A). Temsirolimus pretreatment effectively attenuated HBO-induced neuronal hyperexcitability in both regions; however, the protective effect was significantly more pronounced in the hippocampus than in the temporal cortex (Fig. 8(b)). This regional disparity likely reflects both the differential distribution of mTOR pathway components and their functional specialization across brain areas [56,57].

The hippocampus, widely regarded as the "epicenter" of temporal lobe epilepsy (TLE) and the neuropathological cornerstone of hippocampal sclerosis, exhibits heightened vulnerability to insults and a heightened propensity for aberrant discharge generation [58]. As the primary seizure-onset zone in TLE (a common focal epilepsy syndrome marked by pathological hyperexcitability within the temporal lobe), the hippocampus plays a critical role in initiating abnormal synchronous firing and fostering recurrent, unprovoked seizures [59]. In this study, HBO likely induced initial injury to hippocampal neurons, leading to subsequent activation throughout the temporal lobe and potentially eliciting TLE-like hyperexcitation.

To further investigate whether temsirolimus affects neuronal activation in different brain regions by targeting the mTOR pathway, we performed costaining experiments for c-Fos and mTOR in the brain tissues of mice treated with this drug (Fig. 8). Although mTOR expression was observed throughout the brain, neuronal activation marked by c-Fos was specifically concentrated in the hippocampal and cortical regions (Figs. S28 and S29 in Appendix A), suggesting that these two brain areas may be regulated by

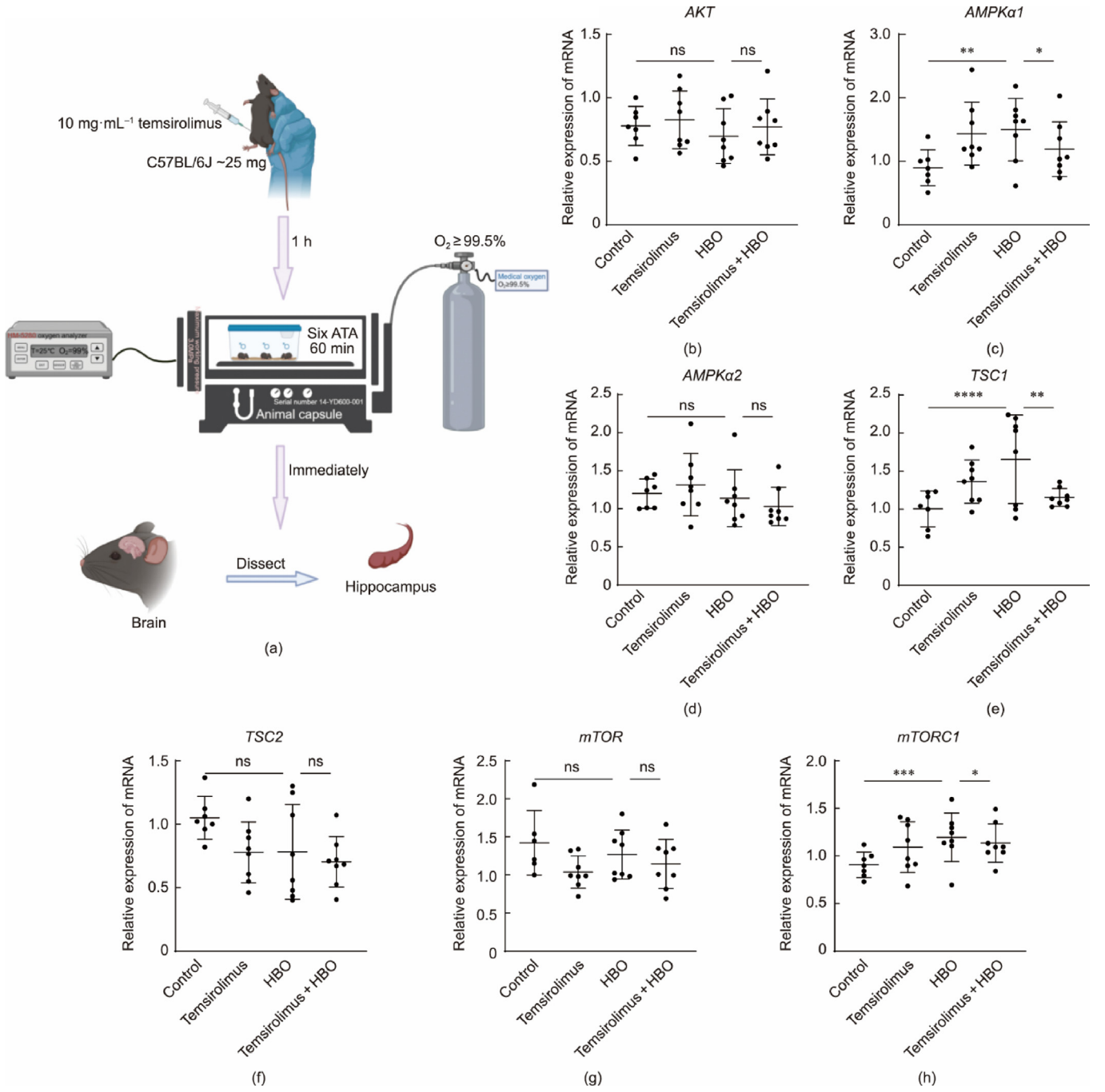

Fig. 7. (a) Schematic diagram of the animal experiment. (b–h) Expression of mTOR pathway-related genes in mouse brain tissue: (b) *AKT*; (c) *AMPKα1*; (d) *AMPKα2L*; (e) *TSC1*; (f) *TSC2*; (g) *mTOR*; (h) *mTORC1*. $^{*}P < 0.05$, $^{**}P < 0.01$, $^{***}P < 0.001$, and $^{****}P < 0.0001$.

the mTOR pathway and thus involved in the process of neuronal activation. However, although neuronal activation in the hippocampal region was significantly inhibited after temsirolimus treatment, the inhibitory effect on mTOR itself was not remarkable.

To further explore this phenomenon, we analyzed the expression of 8-OHdG, a specific DNA damage product resulting from ROS-induced DNA attack [60]. The results revealed that sustained mTOR activation led to a widespread increase in 8-OHdG expression, which was predominantly concentrated in the temporal lobe region, while temsirolimus treatment alleviated such oxidative DNA damage (Fig. S30 in Appendix A). Notably, a bidirectional feedback loop exists between 8-OHdG and the mTOR pathway: excessive ROS-induced mTOR overactivation can upregulate 8-OHdG expression, while 8-OHdG itself can also suppress mTOR expression, thereby inhibiting cellular anabolism and activating autophagy to mitigate damage [61,62]. The inhibitory effect of temsirolimus on 8-OHdG may interfere with the negative feedback regulation of mTOR by 8-OHdG, which could explain the reasons for the insignificant change in mTOR activity.

Seizure-induced neuronal damage is mediated through multiple mechanisms, among which oxidative stress plays a central role. Excessive ROS production coupled with compromised antioxidant defenses synergistically exacerbates neural impairment, with the hippocampus being particularly susceptible to damage because of its high metabolic demand and unique cytoarchitecture [63]. This inherent vulnerability creates a vicious cycle: initial hippocampal

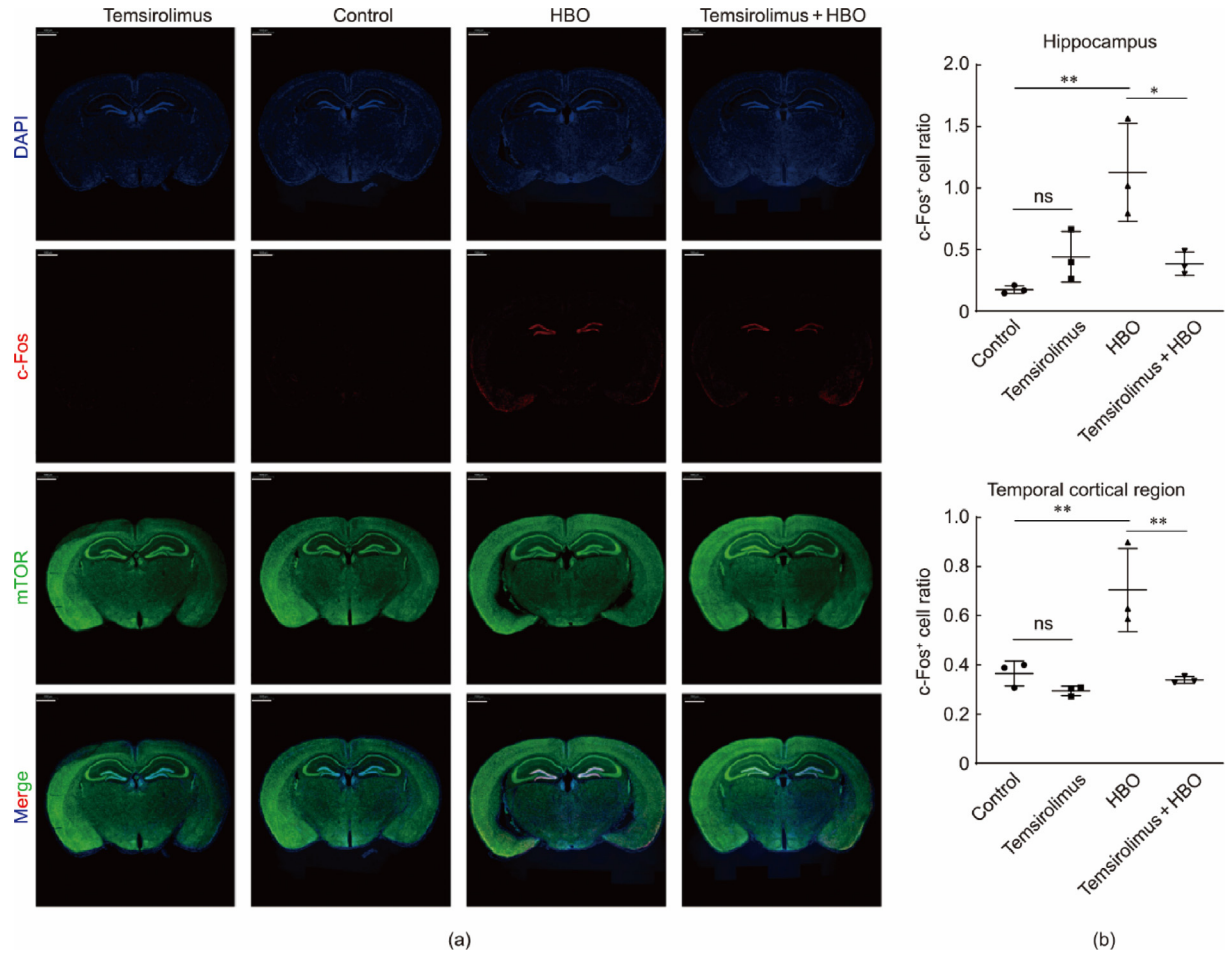

Fig. 8. (a) c-Fos and mTOR costaining of mouse brain tissue. Scale bars, 1000 μm. (b) Quantification of c-Fos$^+$ cells in the hippocampus and temporal cortical region. $^*P < 0.05$, $^{**}P < 0.01$.

damage predisposes to TLE, and recurrent seizures further aggravate hippocampal degeneration. In this study, temsirolimus appeared to confer dual protection by concurrently attenuating mTOR hyperactivation and 8-OHdG accumulation, thereby safeguarding hippocampal and cortical neurons from HBO-induced excitotoxicity and disrupting this self-perpetuating cycle of injury.

In summary, on the basis of the characterization of neuronal activation, temsirolimus has demonstrates significant therapeutic effects on HBO-induced abnormal neuronal excitation.

4. Conclusions

CNS-OT represents a critical challenge in the field of HBOT, necessitating the elucidation of its pathological mechanisms and the development of preventive strategies. This study innovatively employed human cerebral organoids coupled with animal validation to systematically decipher HBO-induced neurotoxicity mechanisms, establishing both novel methodological frameworks and theoretical foundations for CNS-OT research.

Through functional validation, we successfully established a cerebral organoid model system recapitulating the characteristic structural and functional features of the human brain. Integrated sequencing analysis and functional studies elucidated the pivotal role of mTOR signaling in HBO-induced CNS-OT, demonstrating that coordinated activation of the PI3K–AKT and AMPK pathways serves as the key upstream event triggering mTOR hyperactivation. Crucially, these findings were rigorously validated in mouse models: pretreatment with temsirolimus (mTOR inhibitor) significantly mitigated HBO-induced neural damage at the behavioral, molecular, and functional levels, supporting the central regulatory role of the mTOR pathway.

Animal models have been extensively employed in studies of HBO-induced neural injury because of their ability to evaluate systemic and tissue-level physiological responses. However, precise dissection of cell type-specific mechanisms requires targeted labeling and complementary *in vitro* validation. This study established cerebral organoids with structural and functional features of the human brain to recapitulate neurodevelopmental stages and simulate the complex CNS microenvironment, thereby systematically elucidating HBO-induced neurotoxicity mechanisms. Unlike conventional models, cerebral organoids retain human genetic identity while incorporating three-dimensional cytoarchitecture and multicellular interactions, offering a unique platform for investigating CNS-OT and other neurological disorders. We further demonstrate the therapeutic potential of mTOR inhibitors in mitigating HBO-related damage and propose an organoid-based experimental framework for oxygen toxicity research. These findings provide novel mechanistic insights and conceptual advances for the prevention and clinical management of oxygen toxicity, supporting the safe application of HBOT.

Despite these significant advances, our study has certain limitations: the inherent heterogeneity of whole-brain organoids may affect region-specific investigations, and the pharmacological intervention protocol requires further optimization. Future

research should focus on ① refining drug administration regimens to enhance cortical protection; ② developing precise therapeutic strategies targeting hippocampal-cortical circuit specificity; and ③ utilizing juvenile animal models, extended organoid culture (e.g., beyond 120 d), and maturation-induction approaches—such as vascular endothelial cell coculture or modulation of glial differentiation factors—to systematically evaluate structural, functional, and transcriptomic alignment between model systems and both developing and adult CNS. These efforts will advance CNS-OT research toward more precise and effective interventions.

Data availability

Data deposition: The sequences reported in this paper have been deposited in the NCBI Sequence Read Archive under accession number PRJNA1327832.

CRediT authorship contribution statement

Xiaoying Ma: Writing – original draft, Visualization, Methodology, Investigation, Data curation, Conceptualization. **Ye Bai:** Writing – original draft, Validation, Investigation, Data curation. **Jiahui He:** Writing – original draft, Visualization, Validation, Data curation, Conceptualization. **Yunxia Guo:** Writing – review & editing, Validation, Methodology, Data curation. **Miao Meng:** Writing – review & editing. **Sergey M. Novikov:** Writing – review & editing. **Valentyn S. Volkov:** Writing – review & editing. **Ilya Zavidovskiy:** Writing – review & editing. **Dianhuai Meng:** Writing – review & editing, Project administration. **Yan Huang:** Writing – review & editing, Project administration, Funding acquisition. **Xiaochen Bao:** Writing – review & editing, Supervision, Project administration, Funding acquisition. **Xiangwei Zhao:** Writing – review & editing, Resources, Project administration, Funding acquisition.

Declaration of competing interest

The authors declare that they have no known competing financial interests or personal relationships that could have appeared to influence the work reported in this paper.

Acknowledgments

This research was supported by the National Natural Science Foundation of China (82361138570, 81827901, 81971780, and 32371393), the Open Research Fund of State Key Laboratory of Digital Medical Engineering (2023-M08), the Southeast University (SEU) Innovation Capability Enhancement Plan for Doctoral Students (CXJH_SEU 24143), the Yangzhou City Basic Research Program (Joint Special Project)–Health Sector–Young Researcher Project (2025-3-10), and the Guannan Basic Research Program (Joint Special Project)–Health Sector (2025-1-03).

Appendix A. Supplementary data

Supplementary data to this article can be found online at https://doi.org/10.1016/j.eng.2025.10.020.

References

[1] Hachmo Y, Hadanny A, Abu Hamed R, Daniel-Kotovsky M, Catalogna M, Fishlev G, et al. Hyperbaric oxygen therapy increases telomere length and decreases immunosenescence in isolated blood cells: a prospective trial. Aging 2020;12:22445–56.
[2] Bin-Alamer O, Abou-Al-Shaar H, Efrati S, Hadanny A, Beckman RL, Elamir M, et al. Hyperbaric oxygen therapy as a neuromodulatory technique: a review of the recent evidence. Front Neurol 2024;15:1450134.
[3] Dean JB, Stavitzski NM. The O_2-sensitive brain stem, hyperoxic hyperventilation, and CNS oxygen toxicity. Front Physiol 2022;13:921470.
[4] Arieli R, Eynan M, Ofir D, Arieli Y. Brief screening test of ventilatory sensitivity to CO_2 cannot replace the mandatory test for susceptibility to CNS oxygen toxicity. Mil Med 2014;179(8):926–32.
[5] Mahmoud S, Gharagozloo M, Simard C, Gris D. Astrocytes maintain glutamate homeostasis in the CNS by controlling the balance between glutamate uptake and release. Cells 2019;8(2):184.
[6] Heyboer III M, Sharma D, Santiago W, McCulloch N. Hyperbaric oxygen therapy: side effects defined and quantified. Adv Wound Care 2017;6(6):210–24.
[7] Dean JB, Mulkey DK, Garcia III AJ, Putnam RW, Henderson III RA. Neuronal sensitivity to hyperoxia, hypercapnia, and inert gases at hyperbaric pressures. J Appl Physiol 2003;95(3):883–909.
[8] Chen YL, Zhang YN, Wang ZZ, et al. Effects of adenosine metabolism in astrocytes on central nervous system oxygen toxicity. Brain Res 2016;1635:180–9.
[9] Ciarlone GE, Hinojo CM, Stavitzski NM, Dean JB. CNS function and dysfunction during exposure to hyperbaric oxygen in operational and clinical settings. Redox Biol 2019;27:101159.
[10] Lithopoulos MA, Toussay X, Zhong S, Xu L, Mustafa SB, Ouellette J, et al. Neonatal hyperoxia in mice triggers long-term cognitive deficits via impairments in cerebrovascular function and neurogenesis. J Clin Invest 2022;132(22):e146095.
[11] Farahany NA, Greely HT, Hyman S, Koch C, Grady C, Pa$_S$ca SP, et al. The ethics of experimenting with human brain tissue. Nature 2018;556(7702):429–32.
[12] Tye KM, Deisseroth K. Optogenetic investigation of neural circuits underlying brain disease in animal models. Nat Rev Neurosci 2012;13(4):251–66.
[13] Attwell D, Buchan AM, Charpak S, Lauritzen M, MacVicar BA, Newman EA. Glial and neuronal control of brain blood flow. Nature 2010;468(7321):232–43.
[14] Domachevsky L, Rachmany L, Barak Y, Rubovitch V, Abramovich A, Pick CG. Hyperbaric oxygen-induced seizures cause a transient decrement in cognitive function. Neuroscience 2013;247:328–34.
[15] Silbereis JC, Pochareddy S, Zhu Y, Li M, Sestan N. The cellular and molecular landscapes of the developing human central nervous system. Neuron 2016;89(2):248–68.
[16] Otani T, Marchetto MC, Gage FH, Simons BD, Livesey FJ. 2D and 3D stem cell models of primate cortical development identify species-specific differences in progenitor behavior contributing to brain size. Cell Stem Cell 2016;18(4):467–80.
[17] Uzquiano A, Kedaigle AJ, Pigoni M, Paulsen B, Adiconis X, Kim K, et al. Proper acquisition of cell class identity in organoids allows definition of fate specification programs of the human cerebral cortex. Cell 2022;185(20):3770–88.
[18] Lancaster MA, Renner M, Martin CA, Wenzel D, Bicknell LS, Hurles ME, et al. Cerebral organoids model human brain development and microcephaly. Nature 2013;501(7467):373–9.
[19] Shin M, Ha T, Lim J, An J, Beak G, Choi JH, et al. Human motor system-based biohybrid robot-on-a-chip for drug evaluation of neurodegenerative disease. Adv Sci 2024;11(4):2305371.
[20] Williams K, Foliaki ST, Race B, Smith A, Thomas T, Groveman BR, et al. Neural cell engraftment therapy for sporadic Creutzfeldt-Jakob disease restores neuroelectrophysiological parameters in a cerebral organoid model. Stem Cell Res Ther 2023;14(1):348.
[21] Huang Y, Guo X, Lu S, Chen Q, Wang Z, Lai L, et al. Long-term exposure to cadmium disrupts neurodevelopment in mature cerebral organoids. Sci Total Environ 2024;912:1399–410.
[22] Lancaster MA, Knoblich JA. Generation of cerebral organoids from human pluripotent stem cells. Nat Protoc 2014;9(10):2329–40.
[23] Swanson LW. Mapping the human brain: past, present, and future. Trends Neurosci 1995;18(11):471–4.
[24] Ma H, Chen J, Deng Z, Sun T, Luo Q, Gong H, et al. Multiscale analysis of cellular composition and morphology in intact cerebral organoids. Biology 2022;11(9):1270.
[25] Camp JG, Badsha F, Florio M, Kanton S, Gerber T, Wilsch-Bräuninger M, et al. Human cerebral organoids recapitulate gene expression programs of fetal neocortex development. Proc Natl Acad Sci USA 2015;112(51):15672–7.
[26] Baez LA, Eskridge NK, Schein R. Postnatal development of dopaminergic and cholinergic catalepsy in the rat. Eur J Pharmacol 1976;36(1):155–62.
[27] Campbell BA, Lytle LD, Fibiger HC. Ontogeny of adrenergic arousal and cholinergic inhibitory mechanisms in the rat. Science 1969;166(3905):635–7.
[28] Cavalheiro EA, Defeo MR, Mecarelli O, Ricci GF. Intracortical and intrahippocampal injections of kainic acid in developing rats: an electrographic study. Electroencephalogr Clin Neurophysiol 1983;56(5):480–6.
[29] Defeo MR, Mecarelli O, Ricci GF. Bicuculline- and allylglycine-induced epilepsy in developing rats. Exp Neurol 1985;90(2):411–21.
[30] Demchenko IT, Oury TD, Crapo JD, Piantadosi CA. Regulation of the brain's vascular responses to oxygen. Circ Res 2002;91(11):1031–7.
[31] Liu J, Zhang W, Zhou C, Li M, Wang X, Zhang W, et al. Precision navigation of hepatic ischemia-reperfusion injury guided by lysosomal viscosity-activatable NIR-II fluorescence. J Am Chem Soc 2022;144(30):13586–99.
[32] Zhou J, Tan SH, Nicolas V, Bauvy C, Yang ND, Zhang J, et al. Activation of lysosomal function in the course of autophagy via mTORC1 suppression and autophagosome–lysosome fusion. Cell Res 2013;23(4):508–23.

[33] Huang H, Ouyang Q, Zhu M, Yu H, Mei K, Liu R. mTOR-mediated phosphorylation of VAMP8 and SCFD1 regulates autophagosome maturation. Nat Commun 2021;12(1):6622.
[34] Zoncu R, Bar-Peled L, Efeyan A, Wang S, Sancak Y, Sabatini DM. mTORC1 senses lysosomal amino acids through an inside-out mechanism that requires the vacuolar H^+-ATPase. Science 2011;334(6056):678–83.
[35] Lim LQJ, Adler L, Hajaj E, Soria LR, Perry RBT, Darzi N, et al. ASS1 metabolically contributes to the nuclear and cytosolic p53-mediated DNA damage response. Nat Metab 2024;6(7):1294–309.
[36] Gomez-Sintes R, Dolores Ledesma M, Boya P. Lysosomal cell death mechanisms in aging. Ageing Res Rev 2016;32:150–68.
[37] Boya P, Kroemer G. Lysosomal membrane permeabilization in cell death. Oncogene 2008;27(50):6434–51.
[38] Settembre C, Zoncu R, Medina DL, Vetrini F, Erdin S, Erdin SU, et al. A lysosome-to-nucleus signalling mechanism senses and regulates the lysosome via mTOR and TFEB. EMBO J 2012;31(5):1095–108.
[39] Quadrato G, Tuan N, Macosko EZ, et al. Cell diversity and network dynamics in photosensitive human brain organoids. Nature 2017;545(7652):48–53.
[40] Torbati D, Parolla D, Lavy S. Organ blood flow, cardiac output, arterial blood pressure, and vascular resistance in rats exposed to various oxygen pressures. Aviat Space Environ Med 1979;50:256–63.
[41] Calvert JW, Cahill J, Zhang JH. Hyperbaric oxygen and cerebral physiology. Neurol Res 2007;29(2):132–41.
[42] Ravizza T, Scheper M, Di Sapia R, Gorter J, Aronica E, Vezzani A. mTOR and neuroinflammation in epilepsy: implications for disease progression and treatment. Nat Rev Neurosci 2024;25(5):334–50.
[43] Saxton RA, Sabatini DM. mTOR signaling in growth, metabolism, and disease. Cell 2017;168(6):960–76.
[44] Dehnavi S, Kiani A, Sadeghi M, Biregani AF, Banach M, Atkin SL, et al. Targeting AMPK by statins: a potential therapeutic approach. Drugs 2021;81(8):923–33.
[45] Kim J, Kundu M, Viollet B, Guan KL. AMPK and mTOR regulate autophagy through direct phosphorylation of ULK1. Nat Cell Biol 2011;13(2):132–41.
[46] Rosset C, Oliveira Netto CB, Ashton-Prolla P. *TSC1* and *TSC2* gene mutations and their implications for treatment in tuberous sclerosis complex: a review. Genet Mol Biol 2017;40(1):69–79.
[47] Zhang J, Kim J, Alexander A, Cai S, Tripathi DN, Dere R, et al. A tuberous sclerosis complex signalling node at the peroxisome regulates mTORC1 and autophagy in response to ROS. Nat Cell Biol 2013;15(10):1186–96.
[48] Choi YJ, Di Nardo A, Kramvis I, Meikle L, Kwiatkowski DJ, Sahin M, et al. Tuberous sclerosis complex proteins control axon formation. Genes Dev 2008;22(18):2485–95.
[49] Khan AN, Jawarkar RD, Zaki MEA, Mutairi AAA, Mali SN. Targeting PI3K/AKT/mTOR signalling pathway in non-small-cell lung carcinoma: exploring promising bioactive natural compounds as anti-cancer agents. Chem Phys Impact 2025;10:100793.
[50] Li Y, Xu M, Ding X, Yan C, Song Z, Chen L, et al. Protein kinase C controls lysosome biogenesis independently of mTORC1. Nat Cell Biol 2016;18(10):1065–77.
[51] Benjamin D, Colombi M, Moroni C, Hall MN. Rapamycin passes the torch: a new generation of mTOR inhibitors. Nat Rev Drug Discov 2011;10(11):868–80.
[52] Giandomenico SL, Mierau SB, Gibbons GM, Wenger LMD, Masullo L, Sit T, et al. Cerebral organoids at the air-liquid interface generate diverse nerve tracts with functional output. Nat Neurosci 2019;22(4):669–79.
[53] Papouin T, Dunphy JM, Tolman M, Dineley KT, Haydon PG. Septal cholinergic neuromodulation tunes the astrocyte-dependent gating of hippocampal NMDA receptors to wakefulness. Neuron 2017;94(4):840–54.
[54] Liu GY, Sabatini DM. mTOR at the nexus of nutrition, growth, ageing and disease. Nat Rev Mol Cell Biol 2020;21(4):183–203.
[55] Roskoski Jr R. Properties of FDA-approved small molecule protein kinase inhibitors: a 2020 update. Pharmacol Res 2020;152:107059.
[56] Lyu D, Yu W, Tang N, Wang R, Zhao Z, Xie F, et al. The mTOR signaling pathway regulates pain-related synaptic plasticity in rat entorhinal–hippocampal pathways. Mol Pain 2013;9:64.
[57] Hay N, Sonenberg N. Upstream and downstream of mTOR. Genes Dev 2004;18(16):1926–45.
[58] Thom M. Review: hippocampal sclerosis in epilepsy: a neuropathology review. Neuropathol Appl Neurobiol 2014;40(5):520–43.
[59] Mokhothu TM, Tanaka KZ. Characterizing hippocampal oscillatory signatures underlying seizures in temporal lobe epilepsy. Front Behav Neurosci 2021;15:785328.
[60] Dizdaroglu M, Jaruga P, Birincioglu M, Rodriguez H. Free radical-induced damage to DNA: mechanisms and measurement. Free Radic Biol Med 2002;32(11):1102–15.
[61] Magri L, Galli R. mTOR signaling in neural stem cells: from basic biology to disease. Cell Mol Life Sci 2013;70(16):2887–98.
[62] Tang Y, Yang S, Qiu Z, Guan L, Wang Y, Li G, et al. Rapamycin attenuates H_2O_2-induced oxidative stress-related senescence in human skin fibroblasts. Tissue Eng Regen Med 2024;21(7):1049–59.
[63] Attia GM, Elmansy RA, Elsaed WM. Neuroprotective effect of nilotinib on pentylenetetrazol-induced epilepsy in adult rat hippocampus: involvement of oxidative stress, autophagy, inflammation, and apoptosis. Folia Neuropathol 2019;57(2):146–60.